Hemodynamics Indicates Differences Between Patients With And Without A Stroke Outcome After Left Ventricular Assist Device Implantation

Akshita Sahni *[1], Sreeparna Majee †[1], Jay D. Pal ‡[2], Erin E. McIntyre §[3], Kelly Cao ¶[1] & Debanjan Mukherjee ‖[1]

[1]Department of Mechanical Engineering, University of Colorado Boulder
[2]Department of Surgery, University of Washington Seattle
[3]Division of Cardiothoracic Surgery, University of Colorado, Anschutz Medical Campus

Author preprint for medRxiv

Abstract

Stroke remains a leading cause of complications and mortality in heart failure patients treated with LVAD circulatory support. Hemodynamics plays a central role in affecting risk and etiology of stroke during LVAD support. Yet, detailed quantitative assessment of hemodynamic variables and their relation to stroke outcomes in patients with an implanted LVAD remains a challenge. We present an *in silico* hemodynamics analysis in a set of 12 patients on LVAD support; 6 with reported stroke outcomes and 6 without. We conducted patient-specific hemodynamics simulations for models with the LVAD outflow graft reconstructed from cardiac-gated CT images. A pre-implantation baseline flow model was virtually generated for each case by removing the LVAD outflow graft and driving flow from the aortic root. Hemodynamics was characterized using quantitative descriptors for helical flow, vortex generation, and wall shear stress. Our analysis showed higher average values for descriptors of positive helical flow, vortex generation, and wall shear stress, across the 6 cases with stroke outcomes on LVAD support, when compared with cases without stroke. When the descriptors for LVAD-driven flow were compared against estimated baseline flow pre-implantation, extent of positive helicity was higher, and vorticity and wall shear were lower in cases with stroke compared to those without. The study suggests that quantitative analysis of hemodynamics after LVAD implantation; and hemodynamic alterations from a pre-implant flow scenario, can potentially reveal hidden information linked to stroke outcomes during LVAD support. This has broad implications on understanding stroke etiology, LVAD treatment planning, surgical optimization, and efficacy assessment.

Keywords: *heart failure; left ventricular assist device; stroke; hemodynamics; mechanical circulatory support*

*akshita.sahni@colorado.edu
†sreeparna.majee@colorado.edu
‡jaydpal@uw.edu
§erin.mcintyre@cuanschutz.edu
¶kelly.cao@colorado.edu
‖Corresponding Author: debanjan@colorado.edu

1 Introduction

Heart failure remains a major public health concern, affecting at least 26 million individuals globally [1]. According to latest American Heart Association reports, over 6 million individuals above the age of 20 had advanced heart failure between 2007-2020 within the United States alone [2]. Left ventricular assist devices (LVADs) have emerged as the standard of care for bridge-to-transplant as well as destination therapy (DT), for patients with advanced heart failure [3–6]. Recent developments in LVAD technology have substantially improved durability, reduced postoperative effects, and provided long-term survival [7]. Despite the advances in LVAD technology, ischemic stroke remains a significant cause of morbidity and mortality [8, 9]. Stroke rates after LVAD implantation have been reported across several studies in the range of 11-47% of cases [10–13]. Advancements in understanding and reducing post-implant stroke risks can therefore substantially impact treatment outcomes. One major challenge is that factors that influence post-implant stroke risks in subjects on LVAD support are not well understood pre-implant. Hemodynamics is widely acknowledged to play a key role in governing the risk and etiology of complications during LVAD support [14, 15]. Yet, detailed analysis of 3-dimensional space-time varying flow information compared against actual stroke outcomes in patient cohorts remains sparse. Standard-of-care imaging does not currently provide such detailed flow information; and computational flow modeling has emerged as a viable avenue to comprehensively characterize vascular flow driven by an operating LVAD. A number of prior studies have employed computational fluid dynamics to investigate aortic hemodynamics as a function of LVAD outflow graft anastomosis [16–23]; looking specifically into factors such as characterising hemodynamic patterns, thrombogenicity, and effect of LVAD operation including aortic valve reopening. Vast majority of these analyses focus on hemodynamics post-LVAD implantation, and little is known about analysis of (or comparisons against) hemodynamic information pre-implantation. In a series of prior works, we have developed a computational framework to quantitatively assess a range of hemodynamic descriptors such as helicity, vorticity, wall shear, and energy dissipation both as: (a) function of LVAD outflow graft anastomosis; and (b) differences with an estimated pre-implant flow without an operating LVAD [24, 25]. Here we seek to specifically address how the hemodynamics post-implantation, and hemodynamic alterations from a pre-implant flow scenario, are related to stroke risks post-implantation. For this, we present a retrospective secondary analysis on a 12 patient cohort, with 6 having reported stroke outcomes, and 6 without stroke. Our goal is to quantify detailed differences in hemodynamics between stroke and no-stroke outcomes using commonly used flow descriptors, to elucidate whether hemodynamics holds hidden information pertaining to stroke outcomes in subjects on LVAD circulatory support.

2 Methods

2.1 Patient selection

Patient cases were selected from an existing clinical database of patients undergoing LVAD implantation at the University of Colorado Anschutz Medical Campus. For this study, we utilized de-identified patient data from this database for retrospective secondary analysis. Hence, the study was declared to be exempt from IRB review by the Colorado Multiple Institutional Review Board (COMIRB). For each patient, we collected cardiac gated CT angiography scans with the operating LVAD in place, along with report of clinical findings and key clinical metrics. A total of 12 patient cases were selected for this study. Each selected patient case had both full aortic arch upto first level branch vessels; and the LVAD outflow graft anastomosis visible in the cardiac gated CT scan. Key patient clinical variables used for this study have been listed in Table 1. Cases were categorized into two sets with 6 patients each. The first category included 6 patients who experienced a stroke post LVAD treatment (*identified as a cerebrovascular accident or CVA in this study*); while the second category included 6 patients who did not experience any cerebrovascular incidents post LVAD implantation (*identified using the label non-CVA in this study*). Patients reporting a stroke outcome also underwent non-contrast and contrast enhanced head-neck CT imaging. Time between VAD surgery and head-neck imaging was used as an estimate for time between surgery and stroke (listed in Table 1). Furthermore, as per clinical

records, these patients had no reported levels of aortic valve opening, hence we assumed that the aortic valve was sealed close throughout this study, an assumption that we have discussed at length in our prior works [24, 25].

2.2 Image-based modeling of patient vasculature

The cardiac gated CT angiography scans were used to generate patient-specific 3D vascular models using the open source software tool SimVascular [26]. Specifically, from each patient CT image stack, pathlines were created for the aorta, first generation branch vessels, and the LVAD outflow graft. Thereafter, a 3D model of the vascular region of interest, with the LVAD outflow graft attached in place, was generated by creating planar 2D segmentations of the vessel and LVAD outflow graft lumen, and lofting the segmentations. The workflow for generating the 3D vascular model from CT images is presented for one of the cases (Case C6) in Figure 1. Illustration of all the 12 patient anatomy models is presented in Figure 2, with their de-identified case numbers referring to the original anonymized record IDs used in the study, and the models categorized as *CVA* and *non-CVA*. To ensure that the LVAD outflow graft is reconstructed in a geometrically consistent manner, graft inner diameter was measured at different locations along the graft centerline, and the resulting diameters were verified against known standard values as per manufacturer specifications for the device. The comparison of these diameters is shown in the Supplementary Material. An additional set of 12 models were generated by eliminating the path and segmentations for the LVAD outflow graft for each patient, and re-lofting the arterial network without the LVAD graft. These models were referred to as the *Baseline Model* for each patient case, representative of the vascular geometry before LVAD implantation (*See Figure 1 for schematic illustration*). As established in our prior works [24], the baseline cases were included to generate estimates of arterial hemodynamics prior to LVAD implantation, and compare this pre-implantation flow estimate with post-implantation flow to quantify the hemodynamic alterations experienced due to LVAD operation. The vessel lumen for each of these 24 total models were discretized into a computational grid comprising linear, tetrahedral element, and the maximum edge sizes for each model are listed in Table 2. The edge sizes are informed by mesh refinement and aortic hemodynamic studies reported in several prior works [27, 28].

2.3 Patient-specific hemodynamics modeling

Blood was assumed to be a Newtonian fluid demonstrating a linear relationship between shear stress and strain rate [29], with a constant effective average density of 1.060×10^{-3} g.mm^3 and effective dynamic viscosity 0.004 g.mm^{-1}.sec^{-1}. Vessel walls were assumed rigid, and for the LVAD models the aortic valve was assumed to be closed as stated in Section 2.1. Blood flow through all models was computed by solving the Navier-Stokes equations and the continuity equation for fluid momentum and mass balance respectively, using a Petrov-Galerkin stabilized linear finite element method [30–33]. The computations resulted in spatiotemporally varying velocity and pressure fields in the patient's arterial pathway. For each patient the LVAD outflow graft was assumed to drive uniform continuous flow, mapped onto a parabolic profile across the outflow graft inlet, without any pulse modulation. The VAD flow rate (Q_{VAD}) and Mean Arterial Pressure (MAP) was obtained from patient records (see Table 1), and the Total Arterial Resistance (TAR) was estimated as follows (see Table 2 for estimated values for each patient):

$$TAR = \frac{MAP}{Q_{VAD}} \tag{1}$$

Following this, we assumed that flow into each major branching vessel was approximately proportional to the cross-sectional areas of the vessel outlets, based on the assumption of minimal work [34]. Using this estimated flow distribution targets, the TAR was decomposed to assign individual outlet resistance values to the outlets for each patient model, as illustrated in Figure 1. For the baseline models, the Q_{VAD} was instead imposed as the cardiac output exiting from the aortic valve into the aorta of the model. The Q_{VAD} was mapped onto the aortic inlet face as a parabolic profile function in space; and mapped across time using a previously used physiologic pulse-profile shape [24]. The target flow distribution and vessel outlet resistances to all

other outlet boundary faces were kept the same across the LVAD and baseline models. Table 2 summarizes the resistance values for the first generation arteries for each patient case. Using these boundary conditions, blood flow through each of the 12 patient models with VAD and baseline was simulated for a total duration of 3 seconds, with a numerical integration time-step of 0.001 seconds. Once completed, simulated results for the third second of the total simulation duration were extracted and further post-processed to obtain relevant hemodynamic descriptors.

2.4 Hemodynamic descriptors

For quantitative analysis of the hemodynamics across the 12 LVAD and baseline models, we used Eulerian flow descriptors based on three widely adopted hemodynamic features: helicity, wall shear, and vorticity. Detailed description, rationale, and definitions have been outlined in our prior work [24]. Here, we briefly reproduce key details and definitions for describing our analysis. The first descriptor characterizes helical flow patterns generated due to aortic curvature and tortuosity. We computed a time-averaged localized normalized helicity $\overline{LNH}$ defined as follows [24, 35]:

$$\overline{LNH} = \frac{1}{T}\int_0^T \frac{\underline{\boldsymbol{u}} \cdot (\nabla \times \underline{\boldsymbol{u}})\, dt}{\parallel \underline{\boldsymbol{u}} \parallel \parallel (\nabla \times \underline{\boldsymbol{u}}) \parallel} \tag{2}$$

where $\underline{\boldsymbol{u}}$ is the computed blood flow velocity. Based on the above definition, we further devised a volume integrated helicity metric Φ_H and volume averaged helicity metric $\langle \Phi_H \rangle$ defined as follows for a given range of averaged $\overline{LNH}$ values $[L_1, L_2]$:

$$\Phi_H = \int_\Omega \mathcal{I}\left(\overline{LNH}\right) d\Omega; \tag{3}$$

$$\text{and } \mathcal{I}\left(\overline{LNH}\right) = \begin{cases} \overline{LNH} \text{ if } \overline{LNH} \in [L_1, L_2] \\ 0 \text{ otherwise} \end{cases}; \tag{4}$$

$$\langle \Phi_H \rangle = \frac{\int_\Omega \mathcal{I}\left(\overline{LNH}\right) d\Omega}{\int_\Omega d\Omega}; \tag{5}$$

where the volume averaging operation was conducted on the aortic arch alone, excluding the LVAD outflow graft and the first generation carotid and subclavian branches. As a second hemodynamic descriptor, we used the Q-criteria to characterize extent of vortical structures developed in the aortic arch caused by flow emanating from the LVAD outflow graft. Q-criteria is a quantitative descriptor that mathematically identifies locations where rotational flow dominates straining flow [36]. We computed the Q-criterion value based on computed velocity field $\underline{\boldsymbol{u}}$ as:

$$Q = 0.5\left(\parallel 0.5\left(\nabla\underline{\boldsymbol{u}} - \nabla\underline{\boldsymbol{u}}^T\right) \parallel^2 - \parallel 0.5\left(\nabla\underline{\boldsymbol{u}} + \nabla\underline{\boldsymbol{u}}^T\right) \parallel^2\right) \tag{6}$$

For our analysis, the above definition was used to compute a volume averaged Q-criterion metric $\langle \Phi_Q \rangle$ defined as follows [24]:

$$\Phi_Q = \int_\Omega \mathcal{I}\left(\overline{Q}_{sys}\right) d\Omega; \tag{7}$$

$$\text{and } \mathcal{I}\left(\overline{Q}_{sys}\right) = \begin{cases} \overline{Q}_{sys} \text{ if } \overline{Q}_{sys} \in [\overline{Q}_1, \overline{Q}_2]; \\ 0 \text{ otherwise} \end{cases} \tag{8}$$

$$\langle \Phi_Q \rangle = \frac{\int_\Omega \mathcal{I}\left(\overline{Q}_{sys}\right) d\Omega}{\int_\Omega d\Omega}; \tag{9}$$

where Ω denotes the integration domain, which is the aortic arch region excluding other branches; $\overline{Q}$ denotes the Q-value normalized against the systolic Q-value for the baseline model (at $t = 0.18s$ of the third cycle

of simulated flow). Lastly, we compared the extent of wall shear stresses along the aortic wall by computing the time averaged state of wall shear stress (TAWSS) from the computed flow velocity field $\underline{\boldsymbol{u}}$ as follows:

$$\tau_{avg} = \frac{1}{T}\int_0^T \parallel \mu \left(\nabla \underline{\boldsymbol{u}} + \nabla \underline{\boldsymbol{u}}^T\right) \cdot \underline{\boldsymbol{n}} \parallel dt \tag{10}$$

where $\underline{\boldsymbol{n}}$ denotes the normal vector along the wall of the aorta, and $T = 1.0s$ or one cycle for time averaging. Based on the above definition, a surface averaged TAWSS descriptor was computed as follows:

$$\langle \Phi_t \rangle = \frac{\int_\Gamma \tau_{avg} d\Gamma}{\int_\Gamma d\Gamma} \tag{11}$$

where Γ denotes the surface of the aortic arch lumen, excluding any branching vessels. Readers are referred to our prior work [24, 25] for additional details on each of these hemodynamic descriptors. The descriptors were computed using custom post-processing computer programs written in Python using the Visualization Toolkit (VTK) library, and visualized in Paraview.

3 Results

3.1 Visualization of aortic hemodynamic patterns

Figure 3 illustrates the simulated hemodynamic patterns for the 12 cases with an operating LVAD considered in this study, visualized using streamtubes generated at the $t = 0.18$ second time-point of the third simulation cycle. The top row of Figure 3 depicts all *CVA* cases, and the bottom row depicts all *non-CVA* cases. With a non-functional aortic valve, aortic hemodynamics is driven by the impingement of the LVAD outflow jet on the aorta wall. At the jet impingement point there is a spike in pressure, and post-impingement the flow is highly non-linear with significant vortex generation and transport into the arch and descending aorta. As this flow progresses beyond the impingement point, the curvature and tortuosity of the aorta also generates secondary circulatory flow which ultimately leads to flow helicity, as indicated by the coiling of streamtubes in the aorta in Figure 3. Additionally, the presence of a non-functional aortic valve causes flow stagnation at the root of the proximal aortic arch, indicated by the prominent slow flow zones in Figure 3. The corresponding visualization of the estimated pre-implant or *Baseline* hemodynamics for the 12 models is provided in the Supplementary Material.

3.2 Comparison of helical hemodynamics in the aorta

Analysis and comparison of helical hemodynamics in the aorta was undertaken for the *CVA* cases and the *non-CVA* cases using the descriptors outlined in Section 2.4. Figure 4.a. depicts the computed averaged helicity descriptor $\langle \Phi_H \rangle$ defined in Section 2.4, estimated for positive helicity ranges $[L_1, L_2] = [0.2, 1.0]$, compared between the *CVA* and the *non-CVA* cases considered in this study. The results show a higher mean value for $\langle \Phi_H \rangle$ for *CVA* cases (mean=0.41) compared to *non-CVA* cases (mean=0.37). This indicates that aortic hemodynamics driven by LVAD is potentially associated with greater extent of positively helical flow for cases with a stroke outcome, compared to cases without a stroke outcome. Figure 4.b. depicts the ratio of the computed helicity descriptor $\langle \Phi_H \rangle$ between all models with an operating LVAD and the respective pre-implantation *baseline* models. As observed in our prior work [24], we find that hemodynamics in all models with an operating LVAD has increased positive helicity when compared to the estimated baseline flow (i.e. $\langle \Phi_H \rangle$ ratios for LVAD vs baseline greater than 1.0). Additionally, for the cases considered here, the ratio of $\langle \Phi_H \rangle$ with baseline flow had a higher mean value for cases with a stroke (mean = 1.19) compared to cases without a stroke (mean = 1.09). Figure 4.c. depicts the isosurfaces of LNH values taken at +0.2 and -0.2 for each of the 12 LVAD models. This illustration qualitatively indicates that the extent of helicity varies with patient aorta geometry, and is strongly influenced by the outflow graft anastomosis, as was also observed in our multiparametric study discussed in [24]. The corresponding helicity descriptor values for negative helical

flow were also computed using the definitions stated in Section 2.4, with $[L_1, L_2] = [-1.0, -0.2]$, and the comparison is presented in Supplementary Material. However, unlike positive helicity, we did not observe consistent trends or differences between the *CVA* and the *non-CVA* cases for negative helicity.

3.3 Comparison of vortex structures due to jet impingement

Figure 5 illustrates the comparison of vortical flow driven by the LVAD outflow jet between the *CVA* and *non-CVA* cases, using the averaged vorticity descriptor $\langle \Phi_Q \rangle$ defined in section 2.4, as well as the respective maximum Q-criterion values obtained at $t = 2.18$ seconds. For this analysis, $\overline{Q}_1$ was set at 0.001 and $\overline{Q}_2$ was set at the maximum $\overline{Q}$ ratio with value 1. Figure 5.a. presents the comparison of $\langle \Phi_Q \rangle$ between the *CVA* and the *non-CVA* models; while Figure 5.c. presents the comparison for the maximum Q-criteria values. For both maximum Q and $\langle \Phi_Q \rangle$, we observe a higher mean for the *CVA* models (*mean* $\langle \Phi_Q \rangle = 7218.14$*; mean* $Q_{max} = 879452.000$) when compared against the *non-CVA* models (*mean* $\langle \Phi_Q \rangle = 5106.12$*; mean* $Q_{max} = 304848.000$). This indicates that aortic hemodynamics driven by LVAD is potentially associated with greater extent of vortex dynamics for cases with a stroke outcome, compared to cases without a stroke outcome. Ratio of the averaged vorticity descriptor $\langle \Phi_Q \rangle$ and the maximum Q-criteria value with respect to the pre-implantation *baseline* flow estimate is presented in Figure 5.b. and Figure 5.d. Across all 12 models with an attached LVAD outflow graft, both vorticity descriptors were significantly higher than the corresponding baseline models (all ratios with baseline > 1.0). This indicates that the extent of vorticity generated due to LVAD outflow jet impingement on the aortic wall is greater than vorticity in the aortic arch originating from the aortic jet emanating from aortic valve opening. This trend is also consistent with observations generated in our prior parametric study [24]. Additionally, the mean values for both of these ratios were lower for the *CVA* (*mean ratio* $\langle \Phi_Q \rangle = 2.66$*; mean ratio* $Q_{max} = 3.41$) cases when compared against *non-CVA* cases (*mean ratio* $\langle \Phi_Q \rangle = 3.78$*; mean ratio* $Q_{max} = 4.15$). This suggests that the baseline flow dynamics with normal aortic inlet may have greater extent of vorticity for cases with a stroke outcome when compared to those without a stroke outcome after LVAD implantation. Figure 5.e. illustrates the instantaneous 3-dimensional spatially varying vortical structures visualized as iso-surfaces of the computed Q-criteria taken at $0.1\% Q_{max}$ for all the 12 models with an operating LVAD. Qualitative variations in the vortex structures observed in Figure 5.e. can be attributed to differences in jet impingement owing to varying LVAD outflow graft anastomosis and varying operating VAD flow rates. Additionally, the regions at the root of the arch void of any vortex structures corresponds to regions of flow stasis as also identified in Figure 3.

3.4 Comparison of state of wall shear due to LVAD flow

Figure 6 presents the analysis and comparison of wall shear stress along the aorta endothelial lining across the *CVA*, *non-CVA*, and pre-implantation *baseline* cases. Figure 6.a. presents the averaged wall shear descriptor $\langle \Phi_t \rangle$ as defined in Section 2.4 compared across the 6 *CVA* cases and the 6 *non-CVA* cases. We observe a higher mean value for the averaged wall shear descriptor $\langle \Phi_t \rangle$ for the *CVA* cases (mean = 0.17 g.mm^{-1}.sec^{-2}) as compared to the *non-CVA* cases (mean = 0.14 g.mm^{-1}.sec^{-2}). This indicates that aortic hemodynamics driven by an operating LVAD is potentially associated with generally elevated levels of wall shear along the aorta on an average for cases with a stroke outcome when compared to cases without a stroke outcome. The ratio of the averaged wall shear descriptor between the LVAD models and the baseline models are compared in Figure 6.b. Contrary to the absolute values of $\langle \Phi_t \rangle$, we observe that the ratios with baseline are lower in average for the *CVA* cases (mean = 1.30) when compared to the non-CVA cases (mean = 1.54). These observations suggest that cases with a stroke outcome after LVAD implantation had an elevated state of wall shear under the estimated baseline flow conditions, when compared to cases without a stroke outcome. Figure 6.c. presents a 3-dimensional visualization of the TAWSS distribution along the lumen surface of the aortic arch for the *CVA* and *non-CVA* cases. We observe the expected high wall shear values at the LVAD outflow jet impingement location, extremely low wall shear in the regions of stasis as indicated in Figure 3, and the variation in wall shear distribution patterns depending upon the flow development post-impingement which is a function of LVAD outflow graft anastomosis and VAD flow rate.

4 Discussion

We have conducted a systematic retrospective quantitative comparison of aortic hemodynamics between a small set of subjects who did and did not report a stroke outcome after LVAD implantation. Our analysis comprised two categories of flow information. First, we quantified hemodynamics in the aorta driven by an operating LVAD for these two groups of subjects. Second, we derived an estimate of what aortic hemodynamics in these subjects would have been without LVAD support (*referred to here as the baseline models*). In prior works, we have interpreted these differences using a conceptual two jet flow model for LVAD hemodynamics [24, 25]. Specifically, flow during LVAD operation is driven by a jet moving into the aorta from the LVAD outflow graft, while under normal ventricle operation, the flow into the aorta would be driven by a different jet originating from the systolic opening of the aortic valve. The differences in hemodynamics between these two configurations can be viewed as the hemodynamic alterations experienced by the vascular system of a subject who transitions into LVAD circulatory support. Results from our analysis here show that hemodynamics driven by an operating LVAD, as well as the extent of hemodynamic alterations from an estimated baseline flow, can potentially indicate key differences when compared against stroke outcomes post-LVAD implantation. While we presented evidence of differences in the hemodynamic descriptors between cases with and without stroke, we did not infer broader statistical generalizations owing to the small sample size of 6 patients in each group. This, however, remains a focus of our ongoing investigations using the methodology and analysis developed in this study.

The results also link to a deeper mechanistic interpretation when considering the etiology of stroke in patients on LVAD support, and other vascular pathological features due to an operating LVAD. Ischemic stroke in patients on LVAD support can originate from increased clotting propensity within arterial hemodynamics because of the way flow in the aorta is driven by LVAD outflow jet impingement. Increased thrombogenicity is commonly indicated by higher flow stasis, and less mixing of platelets and underlying biochemical species in the flow. Another source of stroke includes thromboemboli that move into the aorta from the LVAD outflow graft (likely from stagnated blood in the dysfunctional ventricle), and are subsequently transported to the brain leading to a stroke. Hemodynamic features such as helicity and vortex dynamics can play a role in both mechanisms. From a flow physics perspective, higher vorticity can indicate lower extent of stasis and higher helicity can foster greater extent of mixing. Also, increased vortical and swirling flow can increase the chances of finite size thromboembolic particles to move towards the cervical vessels into the brain. Additionally, elevated levels of wall shear stress can indicate more systematic effects in vascular health, beyond mechanisms associated with thrombogenicity and thromboembolisms. These include triggering inflammatory responses, endothelial trauma and dysfunction, atherosclerotic potential, and even influencing hormonal regulation and endocrine signaling [37–39].

The evidence that hemodynamics holds quantifiable hidden information about stroke risks and potential for patients on LVAD circulatory support has broad implications. This could inform future advancements in personalization of LVAD surgical implantation, assessment of LVAD treatment outcome, and monitoring and long-term management of patient health on LVAD support. Specifically, there is major interest in surgical optimization of LVAD implantation, and the findings from this study can be used to develop simulation enabled workflows for such optimization. The hemodynamic information can also be used to advance current understanding of stroke etiology in patients on LVAD support, which can further inform anticoagulation or antiplatelet therapy as well as inform the need for additional imaging and clinical workup. We note that the *in silico* methodology devised here is able to quantitatively extrude the hidden connection between flow and stroke outcomes because of its ability to generate well-resolved space-time varying hemodynamic information post-LVAD implantation. Such detailed flow information is currently unavailable from standard-of-care imaging. 4D flow MRI currently provides the most resolved flow information amongst existing imaging techniques, but most LVADs are currently not MRI compatible. Furthermore, while our analysis is conducted retrospectively for patients who have undergone LVAD implantation, in prior works we have demonstrated that such analysis can be conducted also in form of virtual prospective surgery [24, 25], where several potential graft anastomoses can be evaluated using hemodynamic descriptors as described here. Lastly, the higher

ratios of Q-criteria and wall shear stress with baseline in *non-CVA* cases compared to *CVA* cases hints at higher flow vorticity and shear stress in these particular patients under normal aortic inlet condition. Such information enables linking pre-implantation hemodynamic status to post-implantation stroke risks, which is of high significance in terms of surgical planning and treatment efficacy assessment.

Our study was associated with several underlying assumptions and limitations which are noted here. First, we were unable to incorporate any effect of aortic insufficiency and aortic valve opening, owing to the difficulty in obtaining such information for patient cases. This remains an ongoing question of interest for us, and is not an inherent limitation of the computational framework as any such evidence of valve opening can be easily integrated into our hemodynamics analysis framework presented here. Second, we conducted our study on a relatively small cohort of 12 patients, divided into 6 for each categories (with/without stroke). Currently ongoing efforts are aimed at including more clinical cases into our study, and thereafter conducting more comprehensive statistical analysis and hypothesis testing with the larger sample set of data. Third, our hemodynamics modeling itself was based on standard state-of-the-art assumptions in CFD modeling of large artery hemodynamics. Specifically, they include assumptions of the aorta being rigid walls (effectively assuming that the aorta wall displacements are negligible in determining the state of hemodynamics as described here); and the rheology of blood being linear Newtonian (a widely acknowledged and accepted assumption in large artery hemodynamics modeling, although local elevated shear rates in the jet impingement region may cause fluctuations in rheology which was not accounted for). Fourth, in terms of local hemodynamic effects we have also not accounted for any turbulence closure models that capture local turbulence in flow. This remains an ongoing area of investigation, owing to the higher computational cost and numerical complexities of accounting for turbulence closure models in vascular applications.

5 Concluding remarks

In summary, we have presented a computational retrospective hemodynamic analysis for a cohort of patients with and without a reported stroke outcome after LVAD implantation. Our *in silico* analysis integrated patient CT image-based modeling, finite element computational flow modeling, and clinical and outcomes data. We characterized flow post-implantation, as well as obtained an estimate of pre-implantation flow without an LVAD (referred to as baseline models). We found that across the models considered, descriptors of positive helical flow, extent of vorticity, and extent of wall shear, all had higher average values for cases with a stroke outcome. When compared against estimated baseline flow pre-implantation, extent of alteration in positive helicity was higher in stroke case, while the alteration in vortical flow and wall shear was lower in stroke cases. These observations collectively provide evidence that hemodynamics can reveal quantifiable connections and differences when correlated against stroke outcomes in subjects on LVAD support.

Conflicts of interest

Authors have no conflicts of interest regarding this study and the contents of this manuscript.

Acknowledgements

This work was supported by a University of Colorado Anschutz-Boulder (AB) Nexus Research Collaboration Grant awarded to DM and JP; as well as partially supported by a National Institutes of Health Award (R21EB029736) awarded to DM. This work utilized resources from the University of Colorado Boulder Research Computing Group, which is supported by the National Science Foundation (awards ACI-1532235 and ACI-1532236), the University of Colorado Boulder, and Colorado State University. AS conducted all modeling, simulation, and quantitative analysis for the LVAD models. SM expanded the analysis by including the baseline models. KC supported post-processing of all hemodynamic data from the LVAD models. JP and EM guided study design, patient selection, hemodynamic parameter selection, clinical records interpretation, and clinical interpretation of hemodynamic data. DM designed the study, analysed and interpreted simulation data, and drafted the manuscript in collaboration with AS, SM, KC, EM, and JP. All authors reviewed and finalized the draft, and are in agreement regarding the final content of the manuscript.

References

1. Roger, V. L. Epidemiology of heart failure: a contemporary perspective. *Circulation Research* **128,** 1421–1434 (2021).
2. Tsao, C. W., Aday, A. W., Almarzooq, Z. I., Alonso, A., Beaton, A. Z., Bittencourt, M. S., Boehme, A. K., Buxton, A. E., Carson, A. P., Commodore-Mensah, Y., *et al.* Heart disease and stroke statistics—2022 update: a report from the American Heart Association. *Circulation* **145,** e153–e639 (2022).
3. Rose, E. A., Gelijns, A. C., Moskowitz, A. J., Heitjan, D. F., Stevenson, L. W., Dembitsky, W., Long, J. W., Ascheim, D. D., Tierney, A. R., Levitan, R. G., *et al.* Long-term use of a left ventricular assist device for end-stage heart failure. *New England Journal of Medicine* **345,** 1435–1443 (2001).
4. Slaughter, M. S., Rogers, J. G., Milano, C. A., Russell, S. D., Conte, J. V., Feldman, D., Sun, B., Tatooles, A. J., Delgado III, R. M., Long, J. W., *et al.* Advanced heart failure treated with continuous-flow left ventricular assist device. *New England Journal of Medicine* **361,** 2241–2251 (2009).
5. Starling, R. C., Naka, Y., Boyle, A. J., Gonzalez-Stawinski, G., John, R., Jorde, U., Russell, S. D., Conte, J. V., Aaronson, K. D., McGee, E. C., *et al.* Results of the post-US Food and Drug Administration-approval study with a continuous flow left ventricular assist device as a bridge to heart transplantation: a prospective study using the INTERMACS (Interagency Registry for Mechanically Assisted Circulatory Support). *Journal of the American College of Cardiology* **57,** 1890–1898 (2011).
6. Pagani, F. D., Miller, L. W., Russell, S. D., Aaronson, K. D., John, R., Boyle, A. J., Conte, J. V., Bogaev, R. C., MacGillivray, T. E., Naka, Y., *et al.* Extended mechanical circulatory support with a continuous-flow rotary left ventricular assist device. *Journal of the American College of Cardiology* **54,** 312–321 (2009).
7. Kormos, R. L., Cowger, J., Pagani, F. D., Teuteberg, J. J., Goldstein, D. J., Jacobs, J. P., Higgins, R. S., Stevenson, L. W., Stehlik, J., Atluri, P., *et al.* The Society of Thoracic Surgeons Intermacs database annual report: evolving indications, outcomes, and scientific partnerships. *The Journal of Heart and Lung Transplantation* **38,** 114–126 (2019).
8. Kirklin, J. K., Naftel, D. C., Pagani, F. D., Kormos, R. L., Stevenson, L. W., Blume, E. D., Myers, S. L., Miller, M. A., Baldwin, J. T. & Young, J. B. Seventh INTERMACS annual report: 15,000 patients and counting. *The Journal of Heart and Lung Transplantation* **34,** 1495–1504 (2015).
9. Frontera, J. A., Starling, R., Cho, S.-M., Nowacki, A. S., Uchino, K., Hussain, M. S., Mountis, M. & Moazami, N. Risk factors, mortality, and timing of ischemic and hemorrhagic stroke with left ventricular assist devices. *The Journal of Heart and Lung Transplantation* **36,** 673–683 (2017).
10. Harvey, L., Holley, C., Roy, S. S., Eckman, P., Cogswell, R., Liao, K. & John, R. Stroke after left ventricular assist device implantation: outcomes in the continuous-flow era. *The Annals of Thoracic Surgery* **100,** 535–541 (2015).
11. Willey, J. Z., Gavalas, M. V., Trinh, P. N., Yuzefpolskaya, M., Garan, A. R., Levin, A. P., Takeda, K., Takayama, H., Fried, J., Naka, Y., *et al.* Outcomes after stroke complicating left ventricular assist device. *The Journal of Heart and Lung Transplantation* **35,** 1003–1009 (2016).
12. Acharya, D., Loyaga-Rendon, R., Morgan, C. J., Sands, K. A., Pamboukian, S. V., Rajapreyar, I., Holman, W. L., Kirklin, J. K. & Tallaj, J. A. INTERMACS analysis of stroke during support with continuous-flow left ventricular assist devices: risk factors and outcomes. *JACC: Heart Failure* **5,** 703–711 (2017).
13. Morgan, J. A., Brewer, R. J., Nemeh, H. W., Gerlach, B., Lanfear, D. E., Williams, C. T. & Paone, G. Stroke while on long-term left ventricular assist device support: incidence, outcome, and predictors. *ASAIO Journal* **60,** 284–289 (2014).
14. Bartoli, C. R., Giridharan, G. A., Litwak, K. N., Sobieski, M., Prabhu, S. D., Slaughter, M. S. & Koenig, S. C. Hemodynamic responses to continuous versus pulsatile mechanical unloading of the failing left ventricle. *ASAIO Journal* **56,** 410–416 (2010).

15. Soucy, K. G., Koenig, S. C., Giridharan, G. A., Sobieski, M. A. & Slaughter, M. S. Defining pulsatility during continuous-flow ventricular assist device support. *The Journal of Heart and Lung Transplantation* **32,** 581–587 (2013).

16. May-Newman, K., Hillen, B., Sironda, C. & Dembitsky, W. Effect of LVAD outflow conduit insertion angle on flow through the native aorta. *Journal of Medical Engineering & Technology* **28,** 105–109 (2004).

17. Inci, G. & Sorgüven, E. Effect of LVAD outlet graft anastomosis angle on the aortic valve, wall, and flow. *ASAIO Journal* **58,** 373–381 (2012).

18. Karmonik, C., Partovi, S., Loebe, M., Schmack, B., Weymann, A., Lumsden, A. B., Karck, M. & Ruhparwar, A. Computational fluid dynamics in patients with continuous-flow left ventricular assist device support show hemodynamic alterations in the ascending aorta. *The Journal of Thoracic and Cardiovascular Surgery* **147,** 1326–1333 (2014).

19. Callington, A., Long, Q., Mohite, P., Simon, A. & Mittal, T. K. Computational fluid dynamic study of hemodynamic effects on aortic root blood flow of systematically varied left ventricular assist device graft anastomosis design. *The Journal of Thoracic and Cardiovascular Surgery* **150,** 696–704 (2015).

20. Aliseda, A., Chivukula, V. K., Mcgah, P., Prisco, A. R., Beckman, J. A., Garcia, G. J., Mokadam, N. A. & Mahr, C. LVAD outflow graft angle and thrombosis risk. *ASAIO Journal* **63,** 14 (2017).

21. Prather, R., Divo, E., Kassab, A. & DeCampli, W. Computational fluid dynamics study of cerebral thromboembolism risk in ventricular assist device patients: Effects of pulsatility and thrombus origin. *Journal of Biomechanical Engineering* **143** (2021).

22. Caruso, M. V., Gramigna, V., Rossi, M., Serraino, G. F., Renzulli, A. & Fragomeni, G. A computational fluid dynamics comparison between different outflow graft anastomosis locations of Left Ventricular Assist Device (LVAD) in a patient-specific aortic model. *International Journal for Numerical Methods in Biomedical Engineering* **31,** e02700 (2015).

23. Mahr, C., Chivukula, V., McGah, P., Prisco, A. R., Beckman, J. A., Mokadam, N. A. & Aliseda, A. Intermittent aortic valve opening and risk of thrombosis in VAD patients. *ASAIO Journal* **63,** 425 (2017).

24. Sahni, A., McIntyre, E. E., Pal, J. D. & Mukherjee, D. Quantitative assessment of aortic hemodynamics for varying left ventricular assist device outflow graft angles and flow pulsation. *Annals of Biomedical Engineering* **51,** 1–18 (2023).

25. Sahni, A., McIntyre, E. E., Cao, K., Pal, J. D. & Mukherjee, D. The Relation Between Viscous Energy Dissipation And Pulsation For Aortic Hemodynamics Driven By A Left Ventricular Assist Device. *Cardiovascular Engineering and Technology,* 1–17 (2023).

26. Updegrove, A., Wilson, N., Merkow, J., Lan, H., Marsden, A. & Shadden, S. Simvascular: An Open Source Pipeline for Cardiovascular Simulation. *Annals of Biomedical Engineering* **45,** 525–541 (2017).

27. Les, A. S., Shadden, S. C., Figueroa, C. A., Park, J. M., Tedesco, M. M., Herfkens, R. J., Dalman, R. L. & Taylor, C. A. Quantification of hemodynamics in abdominal aortic aneurysms during rest and exercise using magnetic resonance imaging and computational fluid dynamics. *Annals of Biomedical Engineering* **38,** 1288–1313 (2010).

28. Mukherjee, D., Jani, N. D., Narvid, J. & Shadden, S. C. The role of circle of Willis anatomy variations in cardio-embolic stroke: a patient-specific simulation based study. *Annals of Biomedical Engineering* **46,** 1128–1145 (2018).

29. Ku, D. N. *et al.* Blood flow in arteries. *Annual Review of Fluid Mechanics* **29,** 399–434 (1997).

30. Brooks, A. N. & Hughes, T. J. Streamline upwind/Petrov-Galerkin formulations for convection dominated flows with particular emphasis on the incompressible Navier-Stokes equations. *Computer Methods in Applied Mechanics and Engineering* **32,** 199–259 (1982).

31. Franca, L. P., Frey, S. L. & Hughes, T. J. Stabilized finite element methods: I. Application to the advective-diffusive model. *Computer Methods in Applied Mechanics and Engineering* **95,** 253–276 (1992).

32. Franca, L. P. & Frey, S. L. Stabilized finite element methods: II. The incompressible Navier-Stokes equations. *Computer Methods in Applied Mechanics and Engineering* **99,** 209–233 (1992).

33. Taylor, C. A., Hughes, T. J. & Zarins, C. K. Finite element modeling of blood flow in arteries. *Computer Methods in Applied Mechanics and Engineering* **158,** 155–196 (1998).

34. Zamir, M. in *The physics of pulsatile flow* 67–112 (Springer, 2000).

35. Gallo, D., Steinman, D. A., Bijari, P. B. & Morbiducci, U. Helical flow in carotid bifurcation as surrogate marker of exposure to disturbed shear. *Journal of Biomechanics* **45,** 2398–2404 (2012).

36. Jeong, J. & Hussain, F. On the identification of a vortex. *Journal of Fluid Mechanics* **285,** 69–94 (1995).

37. Hasin, T., Matsuzawa, Y., Guddeti, R. R., Aoki, T., Kwon, T.-G., Schettle, S., Lennon, R. J., Chokka, R. G., Lerman, A. & Kushwaha, S. S. Attenuation in peripheral endothelial function after continuous flow left ventricular assist device therapy is associated with cardiovascular adverse events. *Circulation Journal* **79,** 770–777 (2015).

38. Uzarski, J. S., Scott, E. W. & McFetridge, P. S. Adaptation of endothelial cells to physiologically-modeled, variable shear stress. *PloS One* **8,** e57004 (2013).

39. Millon, A., Sigovan, M., Boussel, L., Mathevet, J.-L., Louzier, V., Paquet, C., Geloen, A., Provost, N., Majd, Z., Patsouris, D., *et al.* Low WSS induces intimal thickening, while large WSS variation and inflammation induce medial thinning, in an animal model of atherosclerosis. *PloS One* **10,** e0141880 (2015).

Figures and Tables

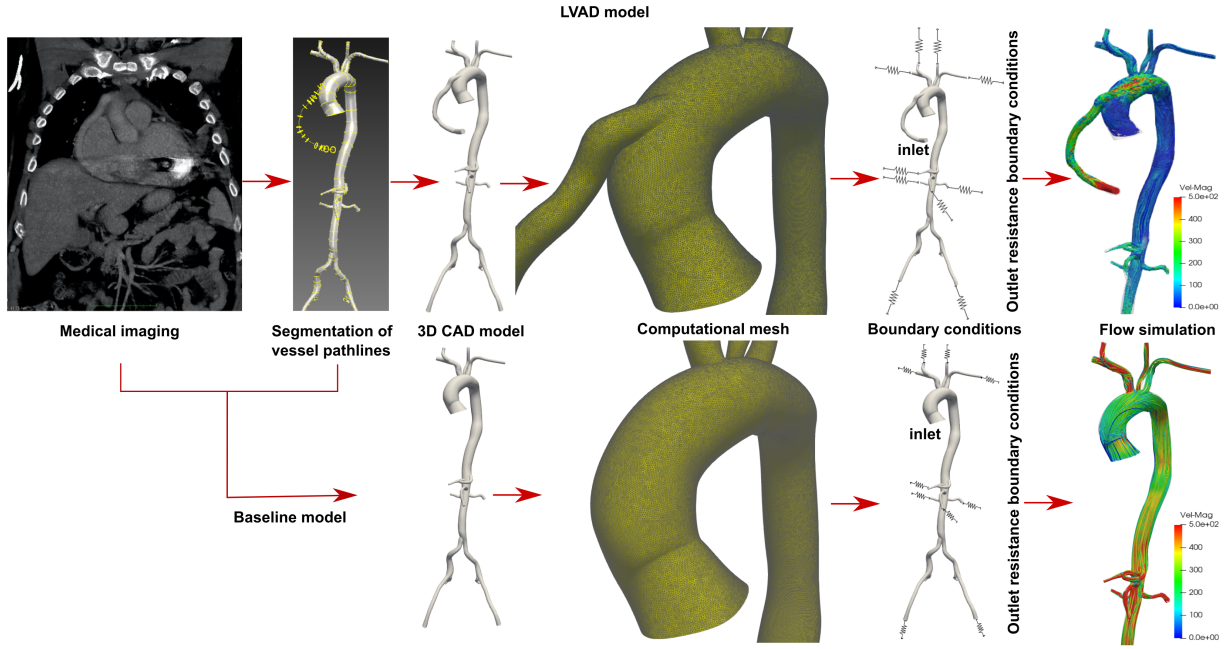

Figure 1: *Schematic overview of the sequence of steps in creating 3D patient vascular models with resistance based outflow boundary conditions from CT image with LVAD graft and baseline model.*

Case	**C1**	**C2**	**C3**	**C4**	**C5**	**C6**	**N1**	**N2**	**N3**	**N4**	**N5**	**N6**
Gender	M	M	F	M	M	M	M	M	F	F	M	M
Age at implant	46-50	61-65	56-60	66-70	36-40	56-60	61-65	61-65	61-65	61-65	56-60	71-75
VAD type†	HM 2	HW	HM 2	HM 3	HW	HW	HM 3	HW	HM 3	HM 3	HW	HM 3
VAD RPM	9400	2500	9000	4800	2560	2720	5700	2720	5500	5600	2700	5400
MAP (mm/Hg)	84	82	66	66	88	90	85	73	92	80	78	78.5
VAD Flow (l/min)	6.9	4.7	4.1	3.8	3.7	3.7	5.3	5.3	3.7	4.0	3.6	4.0
Stroke (CVA)	Yes	Yes	Yes	Yes	Yes	Yes	No	No	No	No	No	No
Time to CVA ($days$)	553*	442	69	1	34	18	–	–	–	–	–	–

Table 1: *A listing of relevant clinical variables for the 12 patient cases included in this study. Gender is indicated as Male (M) or Female (F). The various VAD types (†) are: HM 2 - HeartMate II; HM 3 - HeartMate III; HW - HeartWare. VAD RPM was noted at the time of chest imaging using cardiac gated CT. The Cases listed here, and subsequent tables and figures are used consistently to identify and group patients with respect to stroke and non-stroke outcomes. Time to CVA is estimated in days between LVAD surgery and the first post-stroke head-neck imaging. For case C1; patient needed a pump replacement, and time to CVA was estimated from final pump placement date.*

Case	**C1**	**C2**	**C3**	**C4**	**C5**	**C6**	**N1**	**N2**	**N3**	**N4**	**N5**	**N6**
Stroke (CVA)	Yes	Yes	Yes	Yes	Yes	Yes	No	No	No	No	No	No
Part a.	**Derived total arterial resistance (TAR) ($g.mm^{-4}.sec^{-1}$)**											
Resistance (TAR)	0.10	0.14	0.13	0.14	0.19	0.19	0.13	0.11	0.20	0.16	0.17	0.15
Part b.	**Resistance from branching artery boundary condition ($g.mm^{-4}.sec^{-1}$)**											
R. Subclavian	0.862	1.163	2.144	1.049	1.283	1.772	1.568	0.876	4.690	1.839	0.739	1.008
L. Subclavian	0.810	1.577	2.614	2.654	1.339	3.842	2.045	1.280	6.572	2.629	1.076	1.483
R. Carotid	–	1.981	1.899	2.351	–	2.123	2.470	1.369	3.853	1.154	–	3.843
L. Carotid	0.978	2.126	2.468	2.453	1.334	3.257	3.680	1.630	3.734	1.758	2.948	3.139
Desc. Aorta	–	–	0.274	0.305	0.336	–	0.258	–	0.242	–	0.469	0.359
Celiac Hepatic	1.762	2.219	2.232	3.215	–	8.864	6.775	3.897	–	5.189	–	5.665
Splenic	1.621	1.607	4.007	1.559	–	3.467	1.460	1.157	–	2.029	–	2.936
Sup. Mesenteric	1.257	1.179	1.590	1.247	–	3.051	2.159	1.421	–	2.921	1.672	2.259
R. Renal	2.420	5.076	2.169	–	–	5.939	2.491	1.646	–	4.756	7.470	6.920
L. Renal	1.859	3.441	1.816	–	–	2.262	2.902	1.286	–	2.716	3.543	2.543
R.Ext. Fem.	0.784	0.804	–	–	–	1.164	–	0.826	–	1.656	–	–
L.Ext. Fem.	0.703	0.958	–	–	–	1.154	–	0.720	–	1.827	–	–
R. Profunda	1.837	–	–	–	–	4.456	–	–	–	1.622	–	–
L. Profunda	1.472	–	–	–	–	4.050	–	–	–	1.936	–	–
Part c.	**Spatial and temporal discretization parameters**											
Max. edge size (mm)	0.671	0.775	0.873	0.671	0.715	0.785	0.752	0.814	0.794	0.897	0.837	0.850
Time step size (sec)	0.001	0.001	0.001	0.001	0.001	0.001	0.001	0.001	0.001	0.001	0.001	0.001

Table 2: *A description of all derived hemodynamic parameters that are used for the purpose of specifying the computational hemodynamics simulations for each of the 12 cases studied here. Part a. presents the Total Arterial Resistance (TAR). Part b. represents all the branching artery resistance boundary condition values. Methodology for both are provided in Section 2. Part c. identifies the computational grid/mesh size and time-step size for each model.*

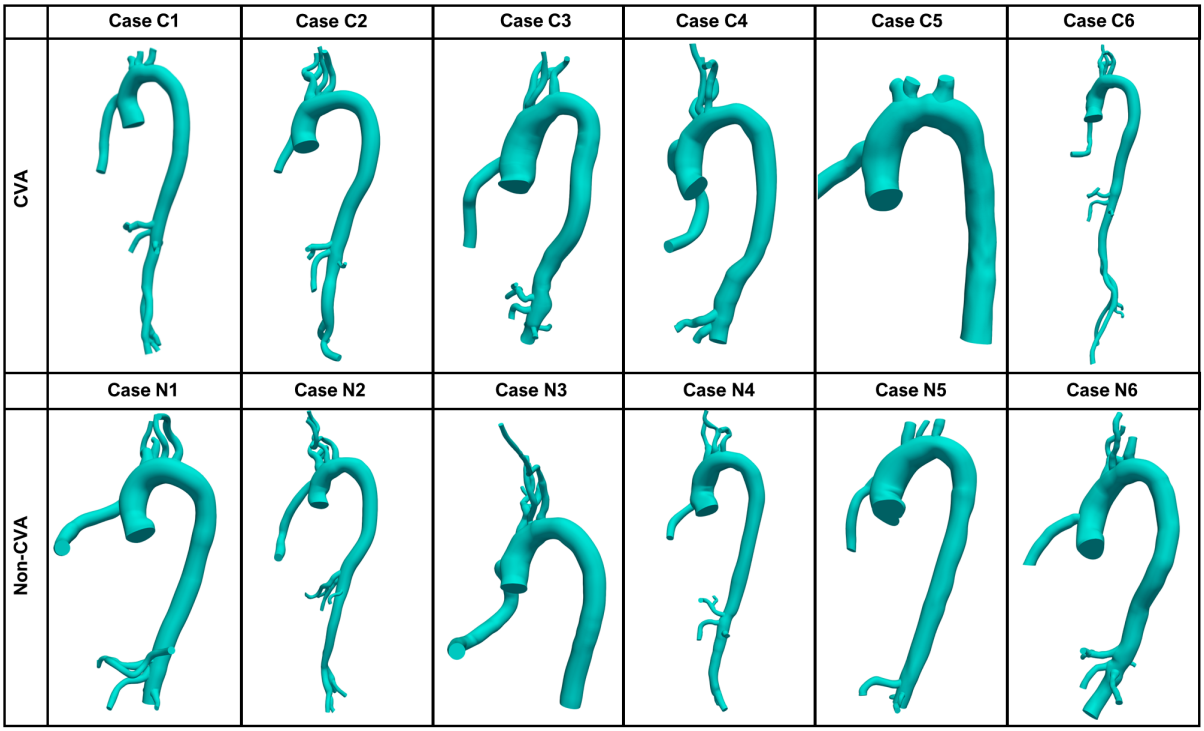

Figure 2: *An illustration of all 12 patient vascular models as reconstructed from CT images, with the LVAD graft of the operational LVAD attached. The Case IDs listed here are the same as identified in Table 1.*

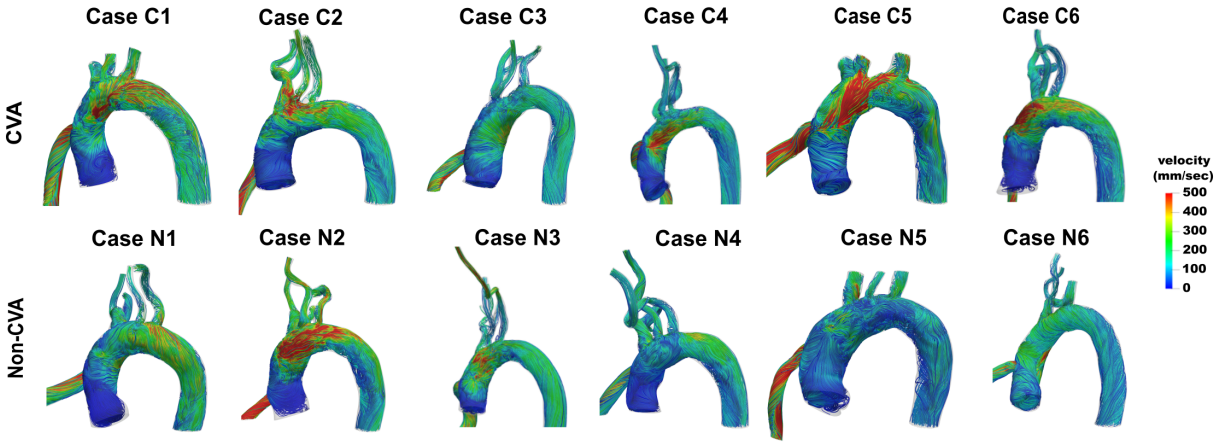

Figure 3: *Visualization of spatially varying aortic hemodynamic patterns using velocity streamtubes illustrated for stroke (CVA) cases at the top and non-stroke (non-CVA) cases at bottom.*

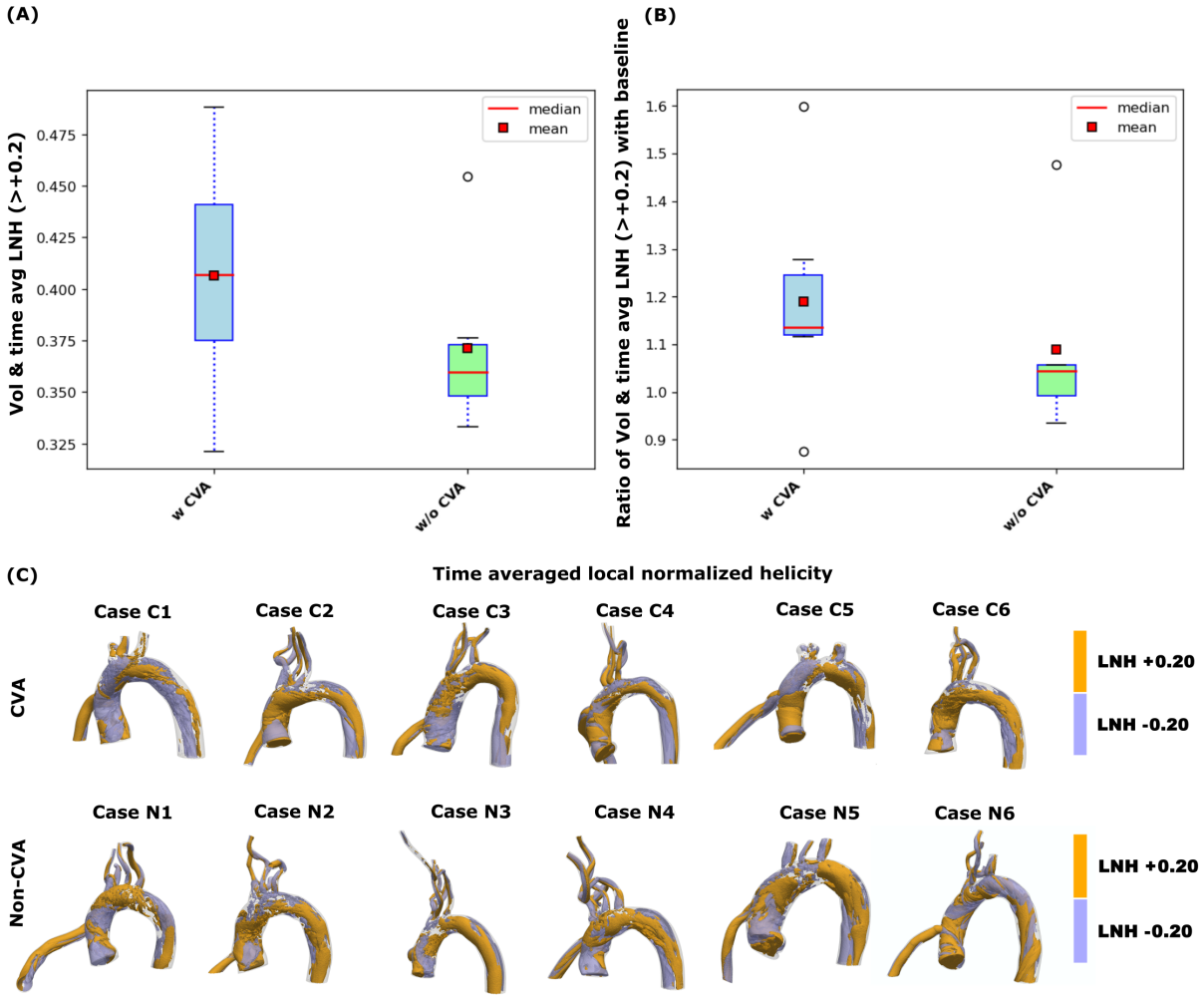

Figure 4: *Comparison between trends in time averaged positive local normalised helicity for CVA vs. non-CVA cases: (A) depicts the extent of helicity for flow with LVAD when computed over the arch volume and across one cardiac cycle; (B) depicts the ratio of positive helicity descriptor with that for the baseline model; and (C) presents isosurface visualisations of time averaged local normalised helicity for CVA and non-CVA cases viewed at* ± 0.20.

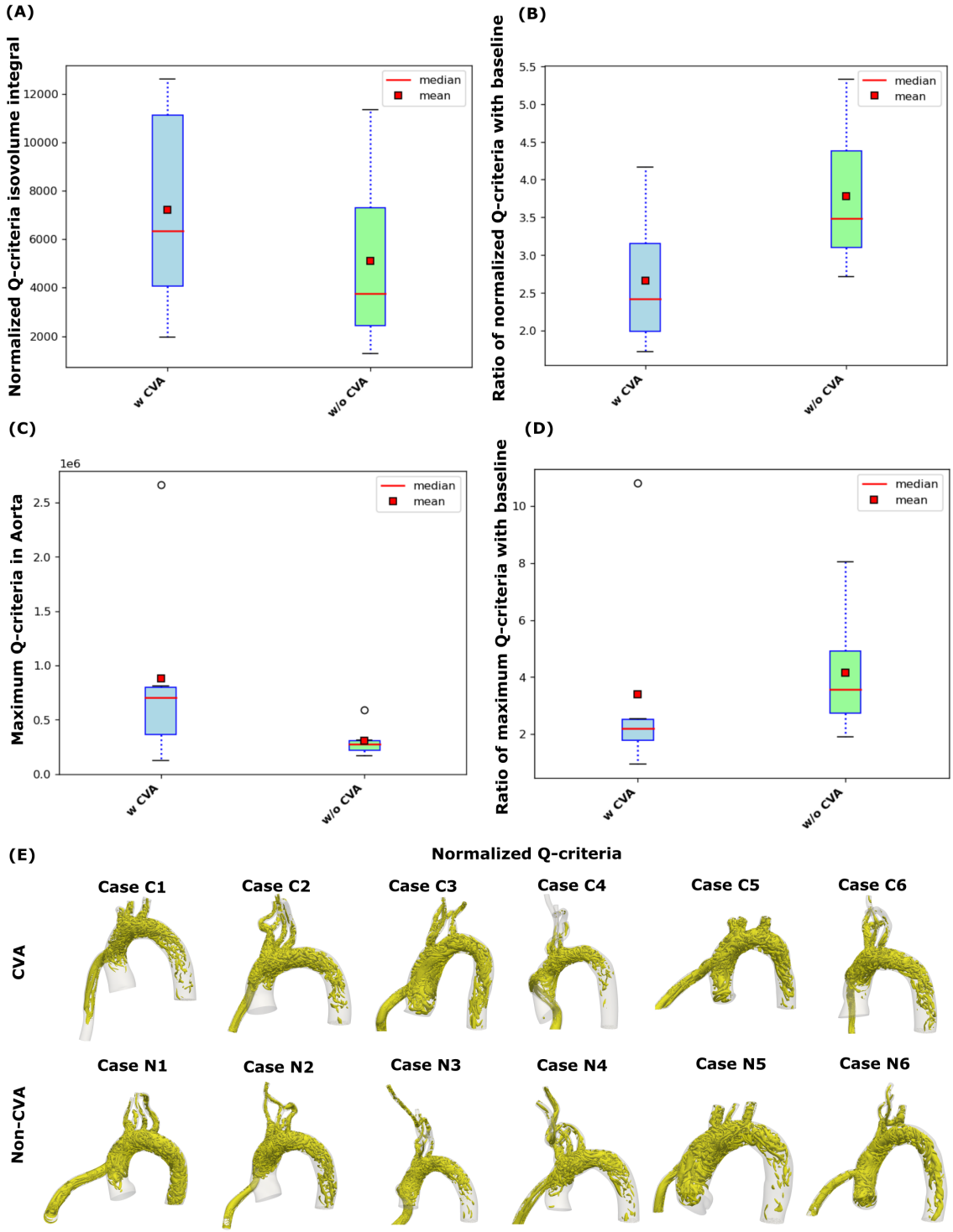

Figure 5: *Comparison between trends in Q-criterion for patients with a stroke(CVA) vs. non-stroke(non-CVA) LVAD outcome: (A) depicts volume averaged normalised Q-criteria, (B) depicts ratio of volume averaged normalised Q-criteria with baseline, (C) depicts the maximum instantaneous Q-criteria (in sec^{-2}) and (D) depicts ratio of maximum instantaneous Q-criteria with baseline at t = 2.18 seconds (E) Isosurfaces of Normalised Q-criteria* $> 0.1\% Q_{max}$ *(in sec^{-2}) for patients with a known stroke or cerebrovascular(CVA) outcome after LVAD deployment(top row) and patients with non stroke/CVA outcome(bottom row).*

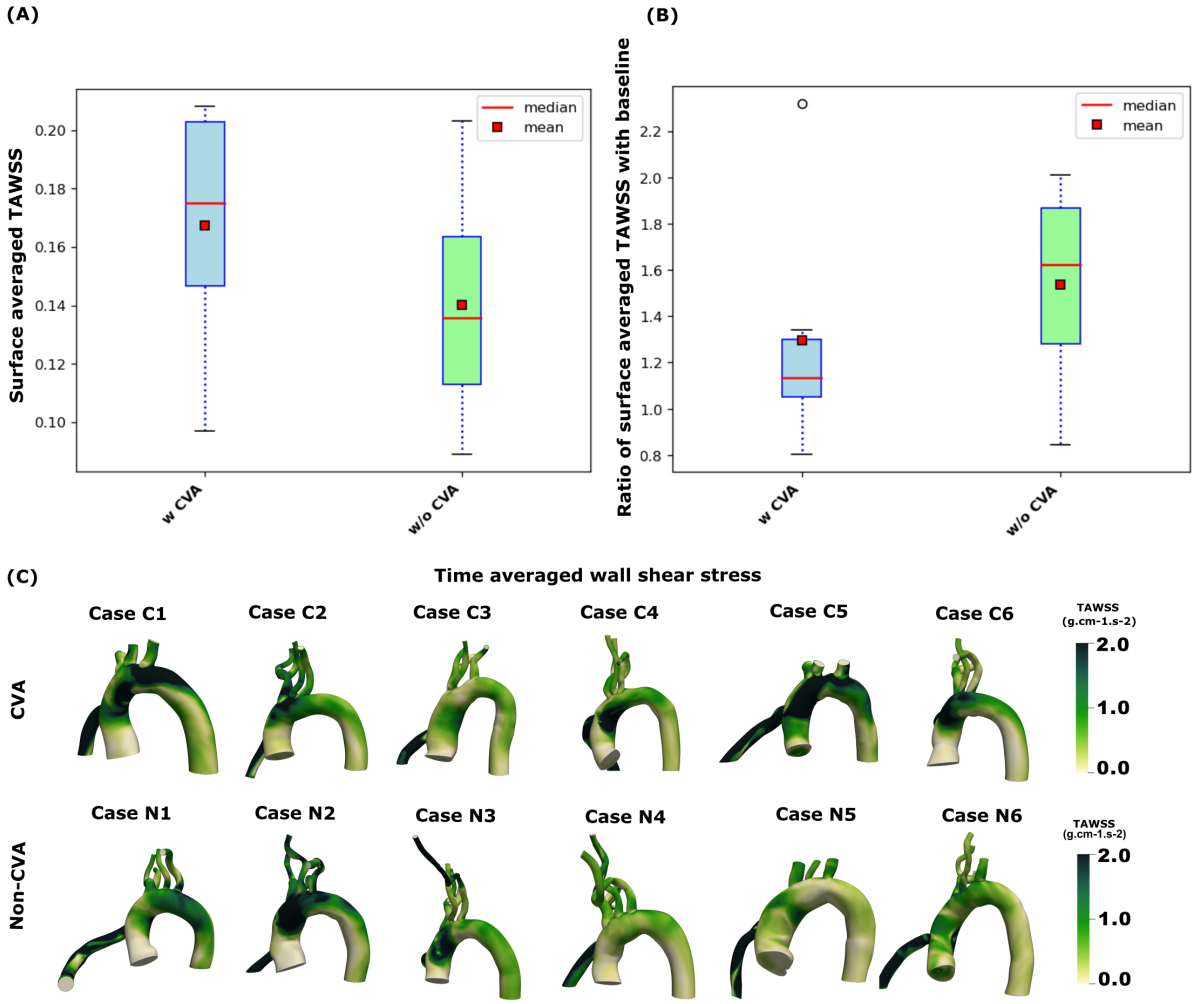

Figure 6: *Comparison between trends in wall shear stress (in units of g.mm^{-1}.sec^{-2}) for CVA vs. non-CVA cases: (A) on the left shows surface and time averaged wall shear stress values with LVAD graft; (B) presents the ratio of surface and time averaged wall shear stress values with that of the baseline models; and (C) illustrates the time averaged wall shear stress (in g.mm^{-1}.sec^{-2}) visualized across the aortic arch, highlighting elevated WSS in the LVAD outflow jet impingement zones.*

Hemodynamics Indicates Differences Between Patients With And Without A Stroke Outcome After Left Ventricular Assist Device Implantation.

Akshita Sahni, Sreeparna Majee, Jay D. Pal, Erin E. McIntyre, Kelly Cao, Debanjan Mukherjee

Supplementary Material Information

S1 Animation of velocity profiles for each patient cases with LVAD

Alongwith the manuscript we have included a separate animation file named *"velocity_compiled.mp4"*,which presents a combined animation of changes in velocity streamtubes with time in over one second of LVAD operation for all 12 patient cases with an attached LVAD graft. This animation provides a temporally varying visualization of the velocity streamtubes, the image for which at $t = 0.18$ sec time instant of the third cycle is presented in Figure 3 of the main manuscript. The animation video is of 14 seconds duration, and considering the LVAD operating cycle as 1 second, the animation is thus rendered 14 times slower than actual LVAD operational cycle.

S2 LVAD outflow graft diameters measured from reconstructed patient models

Figure S1 shows the patient specific LVAD outflow graft inner diameter estimates for all 12 models, measured at different locations along the graft centerline. These diameters were compared with known standard values as per manufacturer specifications for the VAD mentioned in the clinical records of the cases considered. This process and comparison was done to ensure that the LVAD outflow graft for each case is reconstructed in a geometrically consistent manner.

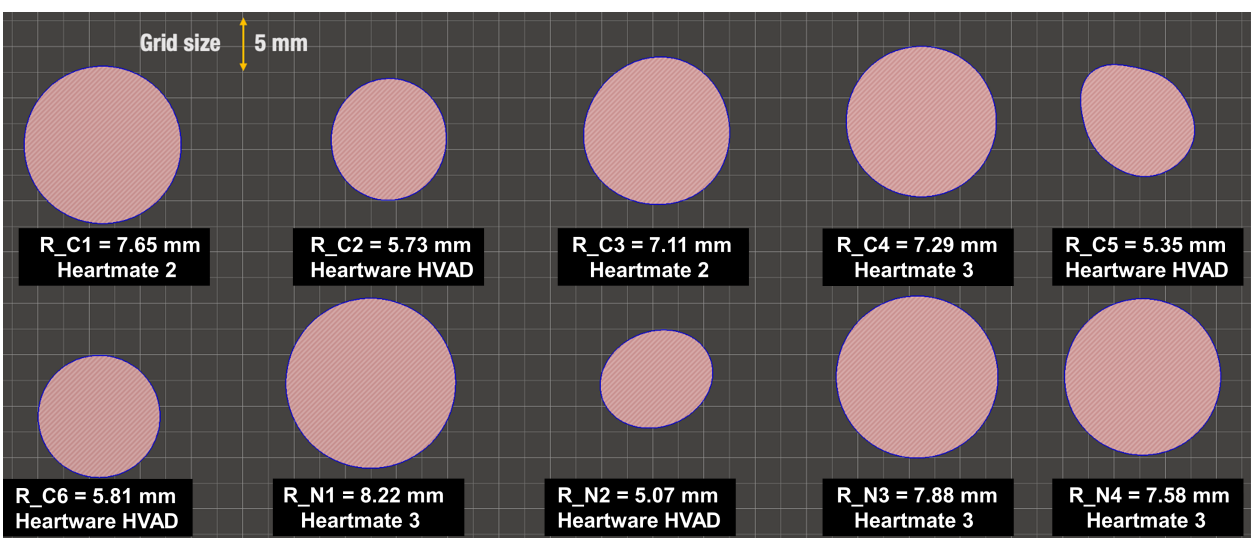

Figure S1: *LVAD outflow graft diameters measured from multiple reconstructed LVAD patient models for verification*

S3 Comparison of negative flow helicity against stroke outcomes

Figure S2, panel A, depicts the time averaged negative helical flow compared between CVA and non-CVA cases, described in the main manuscript, section 3.2. Figure S2, panel B, refers to the ratio of computed averaged helical descriptor $\langle \Phi_H \rangle$ computed between the 12 patient specific LVAD graft models and corresponding baseline models. When compared between CVA and non-CVA cases, we observe that all models with LVAD implant has increased negative helicity when compared to the estimated baseline flow ($\langle \Phi_H \rangle$ ratios for LVAD vs baseline greater than or equal to 1.0). This is similar to the findings for comparison of positive helicity compared with baseline. However, as per the data illustrated in Figure S2 panel A, there were no observable consistent trends in negative helical flow when compared between the CVA and non-CVA cases for aortic hemodynamics driven by the LVAD outflow.

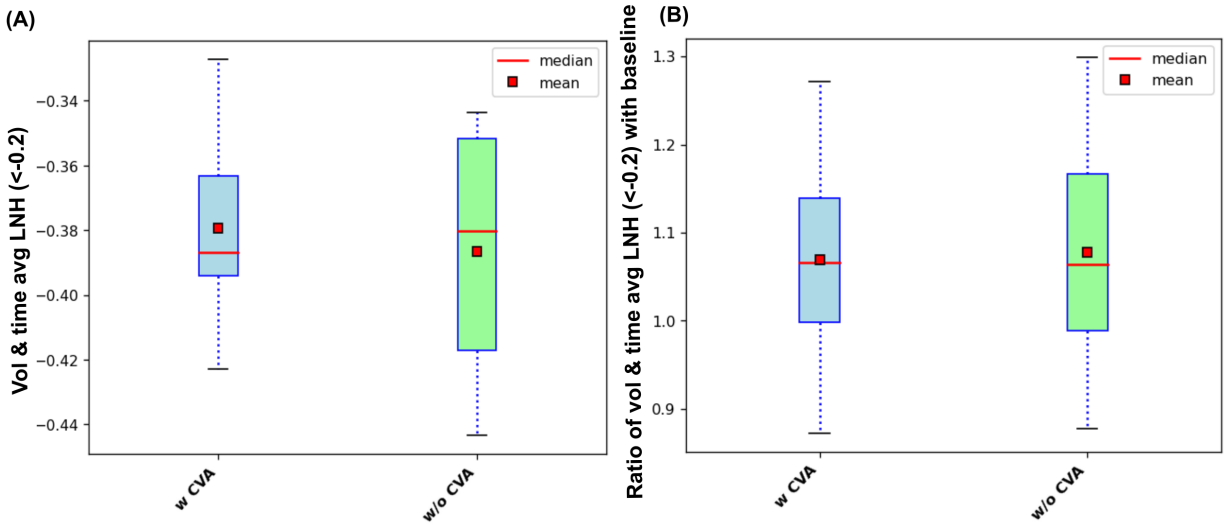

Figure S2: *Comparison between trends in time averaged negative local normalised helicity (LNH) results for CVA vs. non-CVA cases: (A) with LVAD over arch volume and one cardiac cycle, (B) Ratio of negative LNH values with baseline model.*

S4 Visualization of hemodynamic descriptors for baseline models

Here we present additional visualizations for hemodynamics data for the 12 baseline models considered in this study. Figure S3 illustrates the simulated hemodynamic patterns for the 12 baseline cases considered in this study, visualized using streamtubes generated at $t = 0.18$ second time point of the third simulation cycle. We observe that for pre-implantation baseline flow conditions driven by jet flow from the aortic root, the aortic hemodynamics have visibly lesser the vortical and helical flow intensity compared to the corresponding LVAD graft implanted cases (Fig. 3) discussed in Section 3.1. This complements the observations reported in Section 3.2 and Section 3.3. Moreover, the velocity in aortic root for baseline cases are higher, and no prominent flow stasis regions in the aortic root are observed, when compared against the corresponding flow for the LVAD implanted counterpart. Figure S4 depicts the isosurfaces of time averaged LNH contours generated at both +0.2 and -0.2 for each of the 12 baseline models. This additional visualization is included to qualitatively compare with the LNH isosurfaces of 12 LVAD implanted models (Figure 4 (C)). Figure S5 represents a 3-dimensional visualization of the time averaged wall shear stress distribution in the aortic arch for the 12 baseline cases. The wall shear stress is observed to be lower and uniformly distributed all over the aortic arch when compared with TAWSS distribution for cases with LVAD implants as shown in Figure 6 (C).

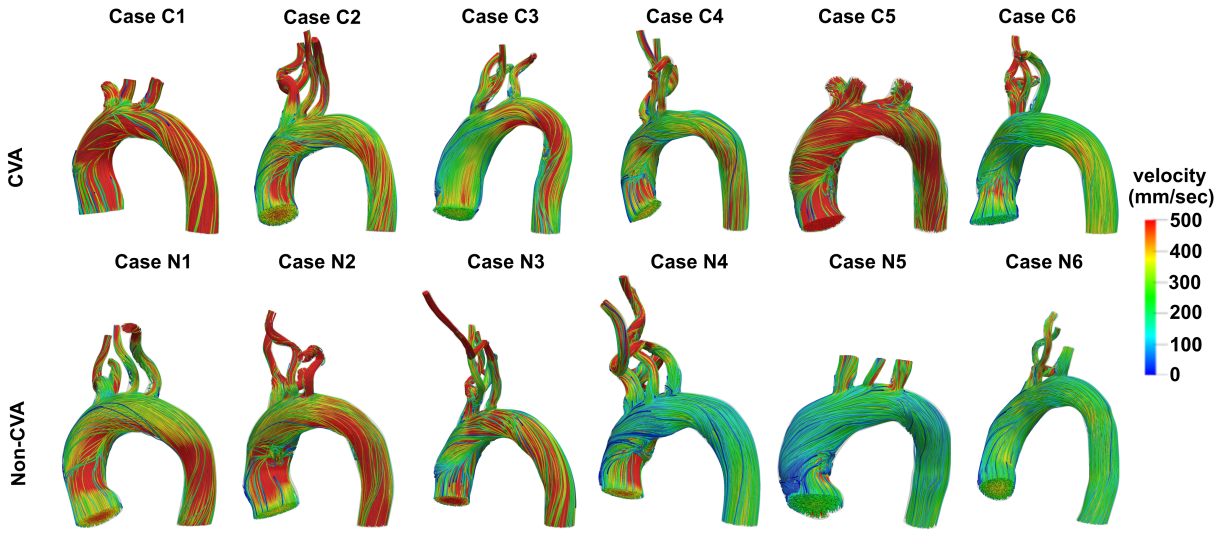

Figure S3: *Velocity streamtubes for the estimated baseline flow for the 12 patient cases included in this study.*

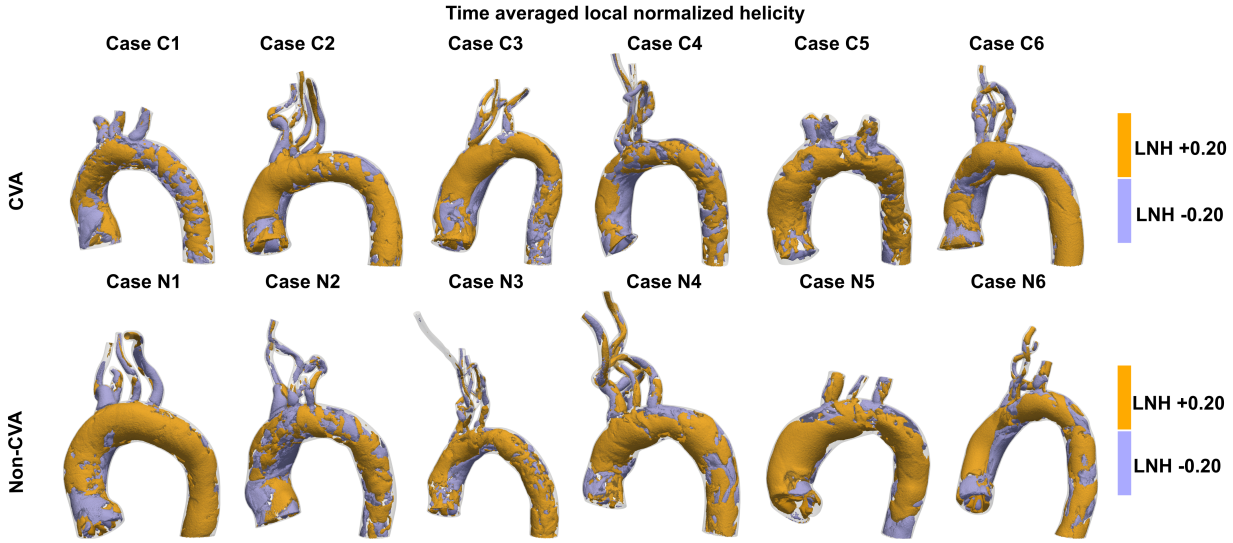

Figure S4: *Isosurface visualisations of time averaged local normalised helicity (LNH) for baseline flow for the 12 patient cases included in this study.*

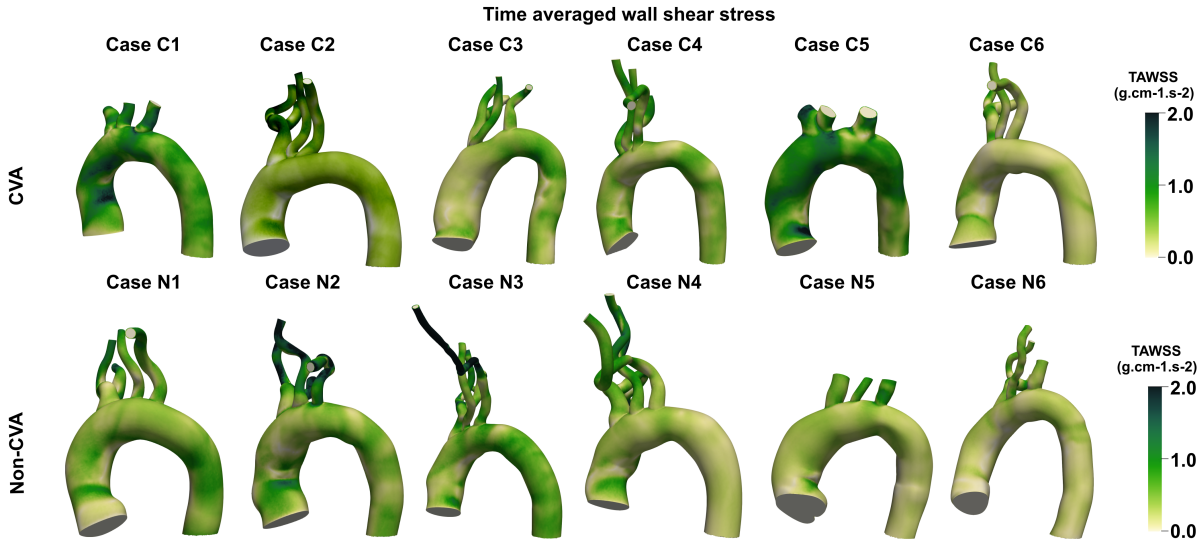

Figure S5: *Visualisation of time averaged wall shear stress over the aortic arch for the baseline flow for the 12 patient cases included in this study.*